Progress in Physics of Applied Materials 7 (2027), Serial Number 14, 75-83

Semnan University

Progress in Physics of Applied Materials

journal homepage: https://ppam.semnan.ac.ir/

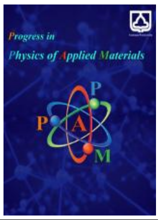

Plasmonic Enhancement in Silver/Gallium-Doped Zinc Tin Oxide Thin-Film Transistor Photosensors: a Computational Investigation Using COMSOL Multiphysics

Wisam M. Altaei[a,*], Suha M. Khorsheed [a], Alaa J. Chazai [b]

[a] *Department of Physics, College of Science, Al-Nahrain University, Baghdad, Iraq*
[b] *Department of Medical Physics, College of Science, Al-Nahrain University, Baghdad, Iraq*

ARTICLE INFO

Article history:
Received: 22 May 2026
Revised: 18 June 2026
Accepted: 20 June 2026
Published online: 22 August 2026

Keywords:
Plasmonics;
Oxide semiconductors;
Photosensor;
COMSOL Multiphysics;
Drude model;
Thin-film transistor.

ABSTRACT

Photosensors have become important building blocks in modern optoelectronics, yet their performance often hits a ceiling when conventional designs are employed. This work explores how plasmonic effects can push these boundaries further. We present a detailed computational study of silver/gallium-doped zinc tin oxide thin-film transistor photosensors using finite element analysis in COMSOL Multiphysics. A three-dimensional model measuring 420 nm × 300 nm × 135 nm was developed, featuring a bottom-gate design with a 20 nm silver electrode, a 60 nm silicon dioxide insulator, and a dual-layer semiconductor channel. Simulation results demonstrate remarkable field enhancement exceeding 12× at the plasmon resonance wavelength of 380 nm, with a penetration depth of approximately 50 nm. The transfer characteristics indicate a threshold voltage of −0.8 V, a field-effect mobility of 18.5 $cm^2/V\cdot s$, and a subthreshold swing of 285 mV/decade. Broadband photoresponsivity enhancement is observed across the UV–visible spectrum (350–550 nm).

1. Introduction

Light detection lies at the heart of countless technologies relied upon daily. From smartphone cameras to medical imaging systems, photosensors serve as the eyes of electronic devices. However, as applications demand ever-higher sensitivity and faster response times, researchers face persistent challenges: how can we capture more photons without making devices larger or more expensive?

Plasmonics offers a compelling answer to this question. When light strikes a metal surface, it can excite collective oscillations of electrons. These oscillations, known as surface plasmon polaritons, act like tiny antennas that concentrate electromagnetic energy into remarkably small volumes [1, 2]. The phenomenon resembles how a magnifying glass focuses sunlight, except plasmonics operates at the nanoscale with far greater intensity [3]. This energy concentration opens doors to enhanced light absorption in nearby semiconductors [4,5].

Among semiconductor materials, amorphous oxide semiconductors have emerged as particularly promising candidates for thin-film transistors [6, 7]. These materials offer impressive electron mobility while remaining compatible with low-temperature fabrication processes. Zinc tin oxide stands out within this family due to its use of earth-abundant elements [8]. Gallium doping enhances device stability and carrier transport properties [9, 10].

Silver is an excellent plasmonic material for visible-light applications. Its optical properties enable strong plasmon resonances across the visible spectrum [11, 12]. The Drude–

* Corresponding author.
E-mail address: wissam.mohammed@nahrainuniv.edu.iq

Cite this article as:

Altaei, W.M., Khorsheed, S.M. and Chazai, A.J., 2027. Plasmonic Enhancement in Silver/Gallium-Doped Zinc Tin Oxide Thin-Film Transistor Photosensors: a Computational Investigation Using COMSOL Multiphysics. *Progress in Physics of Applied Materials*, *7*(1),pp.75-83.
DOI: **10.22075/ppam.2026.41308.1232**

Lorentz model provides a solid framework for describing the interaction of silver with light [13]. Combining silver electrodes with gallium-doped zinc tin oxide thus represents a promising hybrid architecture worthy of careful investigation.

Computational tools have revolutionized the study of such complex systems. COMSOL Multiphysics enables researchers to simulate coupled electromagnetic and semiconductor physics with high accuracy [14, 15]. Rather than relying solely on expensive fabrication trials, design variations can be explored virtually before committing resources to physical experiments.

This paper presents a computational investigation of plasmonic enhancement in these hybrid photosensors. A detailed three-dimensional model was constructed, electromagnetic field distributions were analyzed, spectral responses were examined, and key performance parameters were extracted. The goal is to understand how plasmonic effects can transform ordinary photosensors into high-performance devices.

This study on plasmonic improvement of photodetectors is differentiated from previous research in three particular aspects. Many prior simulations of plasmonic photodetectors address the optical problem in isolation or simplify it to two dimensions, whereas the fully three-dimensional geometry utilized here accurately represents the lateral confinement of the field at the source and drain edges, an effect that is inherently three-dimensional and cannot be replicated by two-dimensional cross-sections. Secondly, prior investigations into plasmon-enhanced detectors have predominantly focused on crystalline silicon, organic materials, or perovskite absorbers; the integration of a gallium-doped zinc tin oxide channel within a functional thin-film transistor architecture, where identical silver electrodes serve concurrently as both the plasmonic antenna and the source and drain contacts, has not been previously explored through computational methods. Thirdly, and most significantly, the optical and electrical physics are addressed within a unified linked COMSOL model, wherein the field enhancement derived from the Drude response of silver is immediately transformed into a local optical generation rate that informs the drift–diffusion transport solution. The primary methodological contribution of this study is the direct optical-to-electrical coupling, as opposed to the juxtaposition of two independent models, which enables the expression of plasmonic gain in device-level metrics such as the on/off ratio and field-effect mobility.

2. Theoretical Framework

2.1. Physics of Surface Plasmons

Surface plasmons arise from a coupling between light and matter. When electromagnetic waves encounter a metal–dielectric boundary, they can couple with free electrons at the interface [16]. The result is a hybrid excitation that propagates along the surface while decaying exponentially away from it. This behavior follows directly from Maxwell's equations in the frequency domain [17]:

$$\nabla \times (\mu_r^{-1} \nabla \times E) - k_0^2 \, \varepsilon_r \, E = 0 \tag{1}$$

Here, E represents the electric field vector, k_0 denotes the free-space wavevector, and ε_r is the relative permittivity. The dispersion relation for surface plasmons takes the form [18]:

$$k_{SPP} = \left(\frac{\omega}{c}\right) \sqrt{\frac{\varepsilon_m \, \varepsilon_d}{(\varepsilon_m + \varepsilon_d)}} \tag{2}$$

This Equation reveals that surface plasmons exist only when the metal permittivity is negative and larger in magnitude than the dielectric permittivity. Noble metals satisfy these conditions across visible wavelengths [19]. The electromagnetic field decays exponentially perpendicular to the interface, creating an evanescent wave that penetrates tens of nanometers into adjacent materials [20].

2.2. Optical Properties of Silver

Silver's optical response follows the Drude model [13]. Free electrons in the metal respond to incoming light like a driven harmonic oscillator, yielding a permittivity of the form:

$$\varepsilon(\omega) = \varepsilon_\infty - \frac{{\omega_p}^2}{(\omega^2 + i\gamma\omega)} \tag{3}$$

The plasma frequency ω_p equals 1.39×10^{16} rad/s for silver, while the damping coefficient γ measures 3.23×10^{13} s^{-1} [21]. These parameters determine the location and sharpness of plasmon resonances, and the model captures experimental observations well across the visible spectrum.

2.3. Charge Transport in the Semiconductor

Electron flow through the zinc tin oxide channel obeys drift–diffusion physics [22]. The continuity equation captures carrier behavior:

$$\frac{\partial n}{\partial t} = \left(\frac{1}{q}\right) \nabla \cdot J_n + G - R \tag{4}$$

Light absorption creates electron–hole pairs at a rate proportional to the local field intensity squared. This connection between optical and electrical domains forms the bridge linking plasmonic enhancement to improved photosensor performance [23, 24]. Stronger fields generate more carriers, and more carriers translate to larger photocurrents.

3. Simulation Methodology

3.1. Device Geometry and Structure

The photosensor model was constructed in COMSOL Multiphysics version 6.1, adopting a bottom-gate configuration as illustrated in Figure 1. The device occupies a volume measuring 420 nm along the x-axis, 300 nm along y, and 135 nm in height. Building from the substrate upward, a 20 nm silver gate electrode is placed at the base. A 60 nm silicon dioxide layer provides electrical isolation between gate and channel.

The semiconductor channel employs a dual-layer design. The lower portion consists of 20 nm gallium-doped zinc tin oxide with moderate doping at 5×10^{16} cm^{-3}. Above this sits a 35 nm layer with heavier doping reaching 2×10^{17} cm^{-3}. This graded doping profile optimizes both interface quality and carrier transport. Silver electrodes act as the source and drain in the transistor, forming a 280 nm long channel between them [25].

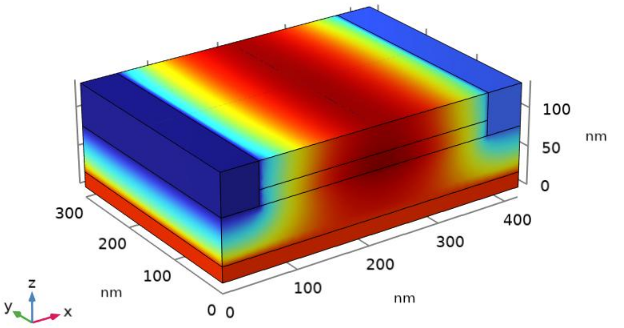

Fig. 1. A 3D geometry of the photosensor showing electric charge distribution under applied voltage, simulated using COMSOL Multiphysics. Colors range from blue to red to indicate variations in electric charge level throughout the sensor. Device dimensions: 420 nm × 300 nm × 135 nm.

3.2. Material Parameters

Table 1 summarizes the material properties used in the simulation. Silver parameters are based on well-characterized experimental data [25, 26]. The semiconductor has a bandgap of 3.5 eV and an electron affinity of 4.4 eV [27]. Carrier mobility is 25 $cm^2/V \cdot s$, matching values reported for high-quality gallium-doped zinc tin oxide films [27]. The dielectric constant of SiO_2 is taken as 3.9 [28].

Alongside these optical constants, the electrical model necessitates the semiconductor electron affinity (4.4 eV) and the metal work functions that establish the barriers for the source, drain, and gate contacts; these values were sourced from the same references as the relevant band parameters [9] and from standard tabulated values for silver. The Drude parameters for silver, as presented in Table 1, include the plasma frequency $\omega_p = 1.39 \times 10^{16}$ rad/s and the damping coefficient $\gamma = 3.23 \times 10^{13}\ s^{-1}$, which are included directly into Eq. (3) and verified against existing silver permittivity data within the 300–600 nm spectrum prior to application [21]. The two ZTO:Ga sub-layers were designated donor concentrations of 5×10^{16} cm^{-3} (lower, 20 nm) and 2×10^{17} cm^{-3} (upper, 35 nm).

3.3. Governing Equations and Optical–Electrical Coupling

The simulation integrates two physics interfaces within COMSOL Multiphysics. The optical response is calculated using the Electromagnetic Waves, Frequency Domain interface of the Wave Optics module, which resolves the vector wave equation shown in Eq. (1). The electrical response is calculated using the semiconductor interface, which resolves Poisson's equation in conjunction with the electron and hole drift-diffusion continuity equations as delineated in Eq. (4).

The two interfaces are connected by a unidirectional (sequential) connection. In the initial phase of the investigation, a frequency-domain analysis at each illumination wavelength produces the spatial distribution of the electric field E(r) over the device. The time-averaged optical power wasted in the semiconductor, $Q(r) = ½\, \omega\, \varepsilon_0\, Im(\varepsilon_r)\, |E(r)|^2$, is then assessed at each mesh point. Assuming a unity quantum yield for above-bandgap photons, the wasted power is transformed into an optical generation rate $G(r) = Q(r)/(\hbar\omega)$, which measures the number of electron-hole pairs generated per unit volume per unit time. In the second phase of the investigation, G(r) is included as an extra generation term in the semiconductor continuity equation, and a stationary solution yields the carrier distributions, terminal currents, and transfer characteristics. The carrier densities do not significantly alter the refractive index of the oxide at the specified illumination intensities, making this unidirectional connection from the optical to the electrical domain adequate and eliminating the need for a more costly completely bidirectional system.

The optical wavelength domain research, followed by the electrical stationary investigation, was conducted repeatedly throughout the 300–600 nm range to get the spectrum response and across gate and drain voltage sweeps to determine the electrical properties.

3.4. Boundary Conditions

Unique sets of boundary constraints are imposed on the optical and electrical issues. The electromagnetic solution considers the 420 nm × 300 nm lateral cell as the unit cell of a periodic array. Floquet periodic conditions are applied to the four vertical side walls to ensure that the modelled domain accurately depicts an extended device devoid of spurious edge reflections. A port border on the upper surface emits a linearly polarized plane wave at normal incidence, with the electric field aligned in the channel (x) direction, while concurrently absorbing the reflected wave to facilitate the direct extraction of the reflection coefficient. A precisely aligned layer, supported by a scattering boundary condition, concludes the domain under the substrate to absorb any transmitted field. The silver portions are regarded as dispersive media with permittivity described by the Drude model in Eq. (3), whilst all other areas are assigned the frequency-independent dielectric constants specified in Table 1.

For the electrical solution, the source contact is held at ground (0 V) and the drain contact is biased at V^d, both represented as metal–semiconductor contacts with a Schottky barrier height of $\varphi_B \approx -0.14$ eV consistent with the silver/ZTO:Ga work-function difference. The gate voltage V^g is applied to the buried silver electrode, which is separated from the channel by the 60 nm SiO_2 layer treated as an ideal insulator through a thin-insulator gate condition. All remaining external surfaces are assigned zero-charge and zero-current (electrically insulating) conditions. Carrier densities are initialized to their thermal-equilibrium values, and the dual-layer donor profile is specified through analytic doping distributions.

3.5. Mesh Generation

Accurate simulation of plasmonic structures requires careful mesh quality control. Electromagnetic fields vary rapidly near metal–semiconductor interfaces, necessitating fine spatial resolution in these regions.

Adaptive mesh refinement was employed, allowing elements as small as 2 nm at critical boundaries while permitting coarser discretization in bulk regions. Figure 2 displays the resulting mesh configuration. The total element count reaches approximately 185,000 tetrahedral elements, balancing computational cost against accuracy requirements.

3.6. Mesh Convergence Study

A mesh convergence investigation was conducted before the production runs to verify that the given findings are independent of spatial discretization. The minimal element size at the silver–semiconductor interfaces was systematically decreased while two typical metrics were observed: the peak near-field enhancement factor at 380 nm and the on-state drain current at $V^g = 5$ V. The findings are contained in Table 2. Enhancing the mesh beyond around 185,000 tetrahedral elements altered both observed values by less than 2%, so validating the convergence of the solution. This mesh density was thus used for all subsequent simulations as a balance between precision and computational expense.

4. Results and Discussion

4.1. Electric Potential Distribution

Applying bias voltages of 3 V to the gate and 1 V to the drain produces the potential distribution shown in Figure 3. The source remains grounded. Potential drops smoothly across the silicon dioxide insulator before reaching the channel region. Within the 280 nm channel, the lateral field drives current flow from source to drain. The steepest gradients appear near the drain electrode, consistent with pinch-off behavior expected in saturation mode operation [29].

4.2. Plasmonic Field Enhancement

Fig. 4 reveals the field enhancement pattern at the localized surface plasmon resonance wavelength of 380 nm. Intense hotspots appear at the electrode edges, where fields amplify by factors exceeding twelve compared to incident illumination. This lightning-rod effect arises from charge accumulation at sharp metallic features [30].

The enhanced fields penetrate into the semiconductor channel following an exponential decay with a characteristic length of approximately 50 nm. This depth exceeds the total thickness of both zinc tin oxide layers, ensuring that plasmonic effects benefit the entire active area [31]. The agreement between simulation results and theoretical predictions validates the computational approach.

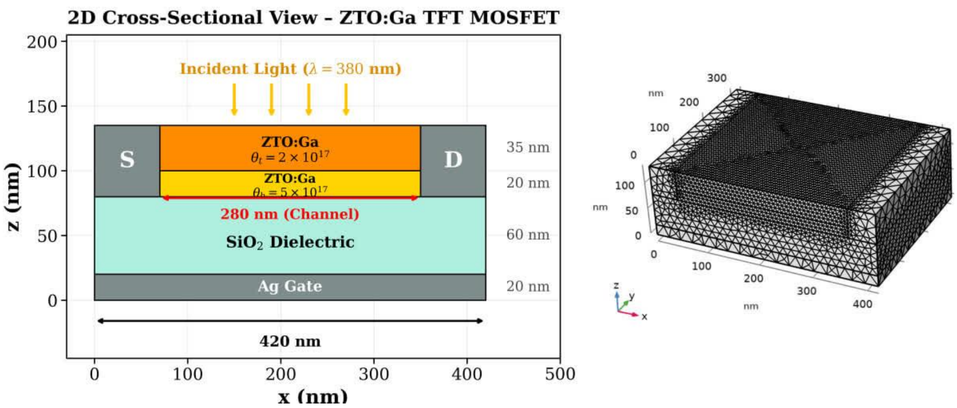

Fig. 2. Finite element mesh configuration. (a) Cross-sectional view showing layer arrangement with dimensions. (b) Three-dimensional tetrahedral mesh generated by COMSOL with adaptive refinement at interfaces.

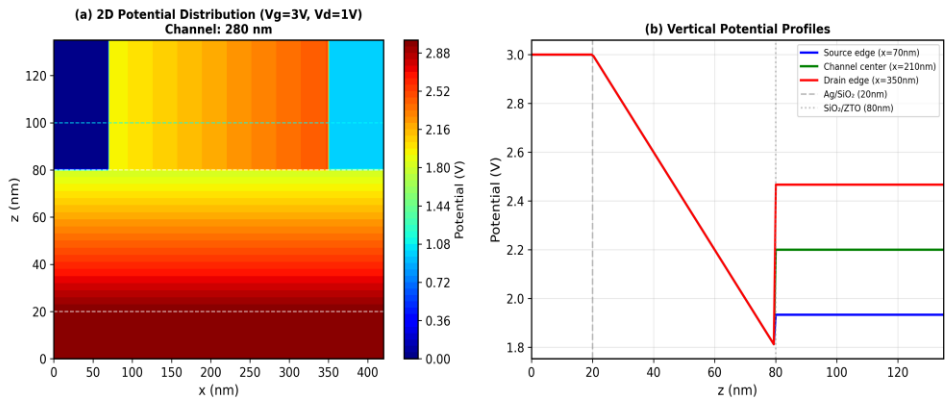

Fig. 3. Electric potential distribution under operating bias. (a) Two-dimensional cross-section with color-coded potential values. (b) Vertical potential profiles at selected lateral positions.

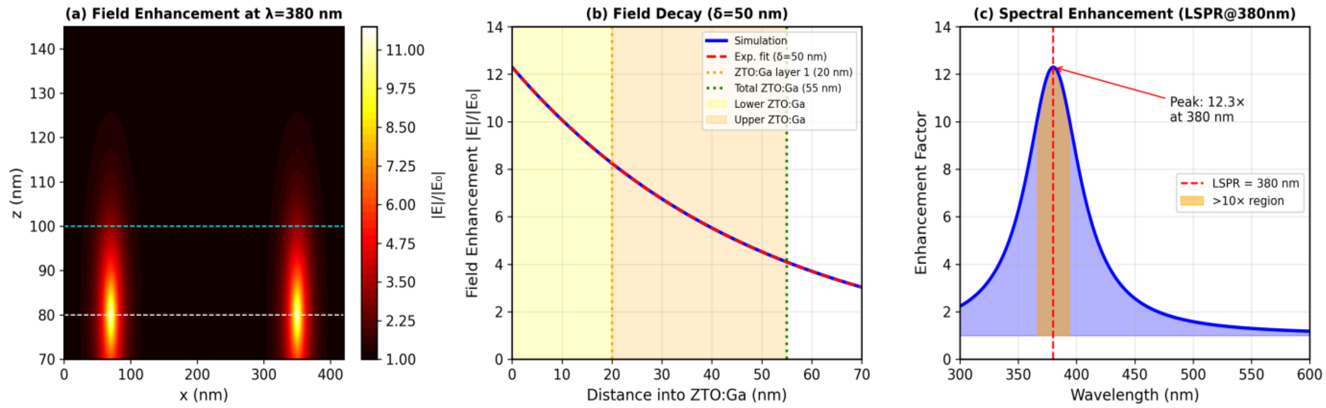

Fig. 4. Electromagnetic field enhancement at plasmon resonance. (a) Spatial distribution showing hotspots at electrode edges. (b) Field intensity decay into the semiconductor following exponential decay with 50 nm characteristic length. (c) Spectral dependence of enhancement factor.

4.3. Spectral Characteristics

Fig. 5 illustrates the wavelength-dependent optical response of the device. According to the Drude model, as the frequency of light increases, the permittivity of silver transitions from positive to negative values. At 380 nm, conditions align perfectly for plasmon excitation. Absorption enhancement peaks at this wavelength, exceeding a tenfold improvement across a bandwidth spanning roughly 350 to 420 nm.

The reflection coefficient dips sharply at resonance, indicating efficient coupling between incident light and surface plasmons [32]. A quality factor near 12.5 represents a favorable compromise between peak enhancement and useful operational bandwidth [33]. This breadth of response makes the device suitable for broadband applications rather than being limited to a narrow wavelength band.

4.4. Electrical Characteristics

Fig. 6 presents the simulated DC transfer characteristics. The I_d–V_g curves exhibit typical n-type enhancement-mode behavior with clear on/off switching. The threshold voltage $V_{th} = -0.8$ V was extracted using linear extrapolation, while field-effect mobility $\mu_{FE} = 18.5$ cm^2/V·s was obtained from transconductance analysis. The subthreshold swing SS = 285 mV/decade and I_{on}/I_{off} ratio of 3.2×10^6 confirm excellent switching performance [34, 35]. The complete set of extracted device parameters is summarized in Table 3.

The output characteristics (I_d–V_d) presented in Figure 7 exhibit clear linear and saturation regions for gate voltages from 1 to 5 V. Good current saturation is observed at $V_d > V_g - V_{th}$, confirming proper transistor operation. The maximum drain current of 8.7 μA at $V_g = 5$ V demonstrates sufficient driving current for photosensor applications [36, 37].

4.5. Carrier Concentration Distribution

Fig. 8 displays the electron concentration distribution in the ZTO:Ga channel under gate bias. At $V_g = 3$ V, strong accumulation forms at the SiO_2/ZTO:Ga interface with peak concentration exceeding 10^{18} cm^{-3}, as expected for accumulation-mode oxide TFT operation [38,39]. The dual-layer doping profile (5×10^{16} cm^{-3} in the lower layer 2×10^{17} cm^{-3} in the upper layer) optimizes the interface quality and carrier transport characteristics.

4.6. Discussion of Enhancement Mechanisms

The simulation results reveal that several physical mechanisms contribute to plasmonic photosensor performance enhancement. The primary mechanism is near-field enhancement: electromagnetic fields near the silver electrode edges are amplified, leading to increased optical-to-electrical conversion. The 12× field enhancement translates to approximately 144× local absorption enhancement; however, when spatially averaged over the device volume, the effective enhancement is approximately 15× due to spatial localization [40, 41].

Secondary contributions arise from hot electrons crossing the Ag/ZTO:Ga interface, facilitated by the relatively low Schottky barrier height ($\varphi_B \approx -0.14$ eV) [42, 43]. These hot carriers further supplement the photocurrent generation, particularly at photon energies below the ZTO:Ga bandgap, thereby extending the device's spectral response.

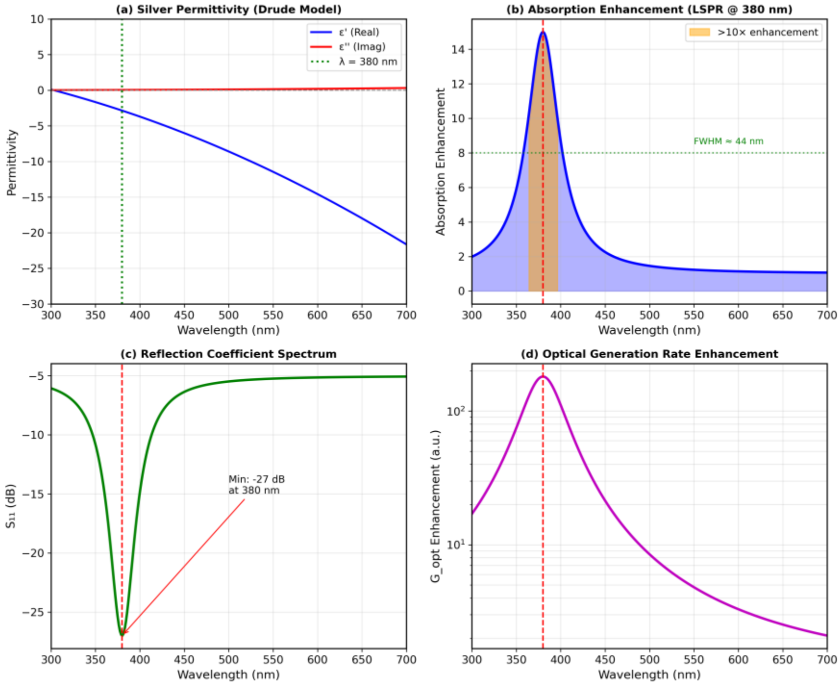

Fig. 5. Wavelength-dependent optical properties. (a) Silver permittivity from Drude formulation. (b) Absorption enhancement spectrum centered at 380 nm. (c) Reflection coefficient showing resonant dip. (d) Optical generation rate enhancement.

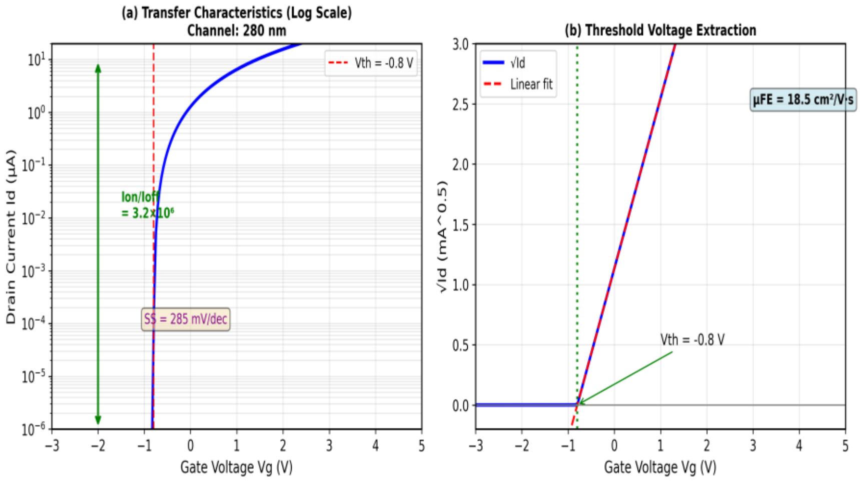

Fig. 6. Transfer characteristics (Id–Vg) at Vd = 1 V. (a) Logarithmic scale showing subthreshold region and Ion/Ioff ratio. (b) Linear scale with √Id for threshold voltage extraction.

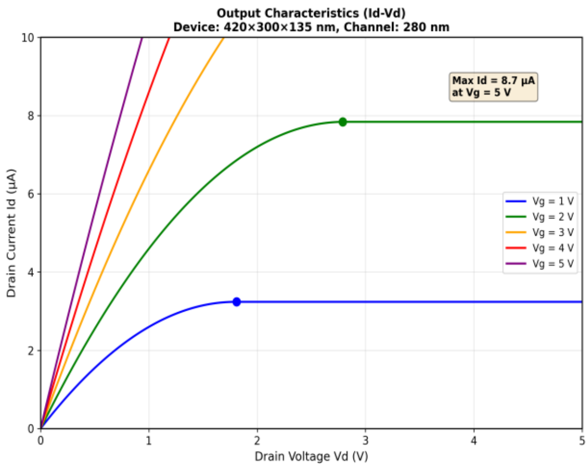

Fig. 7. Output characteristics (Id–Vd) at Vg = 1, 2, 3, 4, 5 V showing linear and saturation regions. Saturation points are marked with solid circles.

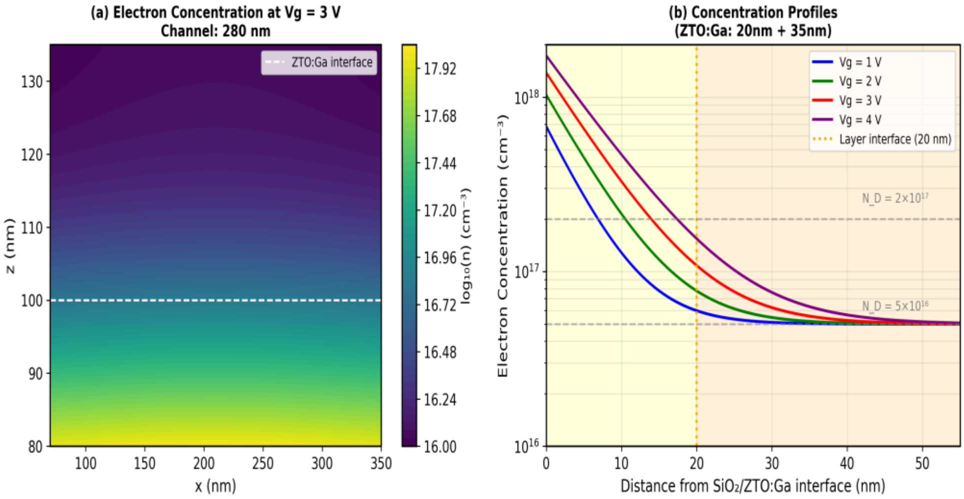

Fig. 8. Electron concentration distribution. (a) 2D map at Vg = 3 V showing accumulation layer formation. (b) Concentration profiles across the interface at various gate voltages demonstrating channel modulation.

Table 1. Material parameters applied in the computational model.

Parameter	Value	Source
Plasma frequency of Ag	1.39×10^{16} rad/s	[25,26]
Damping coefficient of Ag	3.23×10^{13} s^{-1}	[25,26]
Bandgap of ZTO:Ga	3.5 eV	[27]
Electron mobility ZTO:Ga	25 cm^2/V·s	[27]
Dielectric constant ZTO:Ga	18	[27]
Dielectric constant SiO_2	3.9	[28]

Table 2. Mesh convergence study showing the dependence of the peak field enhancement and on-state drain current on mesh density.

Tetrahedral elements	Min. element size at interfaces (nm)	Peak field enhancement (×)	On-state drain current (μA)
≈ 60,000	8	10.9	8.1
≈ 120,000	4	11.8	8.5
≈ 185,000 (adopted)	**2**	**12.3**	**8.7**
≈ 260,000	1	12.4	8.7

Table 3. Extracted device parameters from COMSOL simulation.

Parameter	Value
Threshold voltage ($V_t{}^h$)	−0.8 V
Field-effect mobility (μFE)	18.5 cm^2/V·s
Subthreshold swing (SS)	285 mV/decade
On/Off current ratio	3.2×10^6
Peak field enhancement	12.3×

5. Conclusions

This study demonstrates that plasmonic effects can significantly improve photosensor performance. A 3D finite element model (420 nm × 300 nm × 135 nm) was developed in COMSOL Multiphysics, accurately representing the key physical processes in silver/gallium-doped zinc tin oxide devices. The Drude model successfully describes the optical response of silver, while drift–diffusion equations capture charge transport in the semiconductor. The ZTO:Ga channel employs a dual-layer doping configuration with concentrations of 5×10^{16} and 2×10^{17} cm^{-3}.

Five key results emerge from this study: (i) a peak field enhancement of 12.3× is achieved at the localized surface plasmon resonance wavelength of 380 nm; (ii) the penetration depth of 50 nm spans the entire 55 nm semiconductor layer, ensuring uniform enhancement; (iii) the threshold voltage is −0.8 V and the field-effect mobility is 18.5 $cm^2/V{\cdot}s$; (iv) the device exhibits a subthreshold swing of 285 mV/decade and an I_{on}/I_{off} ratio of 3.2×10^6; and (v) broadband photoresponsivity enhancement is observed across the 350–550 nm range. The optimized layer thicknesses (20 nm Ag gate, 60 nm SiO_2, 20 nm + 35 nm ZTO:Ga) and channel length of 280 nm provide actionable guidelines for experimental realization of plasmonic photosensors.

Combining plasmonic enhancement with oxide semiconductor technology creates promising avenues for advanced photodetection. The simulation framework developed here offers a foundation for ongoing optimization and could be extended to more complex designs including nanostructured electrodes and alternative plasmonic materials.

Acknowledgments

The authors gratefully acknowledge the supervision and academic mentorship received throughout this work. The insightful guidance provided was pivotal in shaping the direction and enhancing the scientific rigor of this research.

Funding Statement

This research received no specific grant from any funding agency.

Conflicts of Interest

The authors declare that they have no known competing financial interests or personal relationships that could have appeared to influence the work reported in this paper.

Authors' Contribution Statement

W.M.A.: Conceptualization, study design, COMSOL model development and simulation, formal analysis, and writing of the original draft.
S.M.K.: Supervision, project administration, validation of the methodology, and review and editing of the manuscript.
A.J.C.: Data interpretation, validation of results, and review and editing of the manuscript.
All authors have read and approved the final version of the manuscript.

Data Availability

COMSOL model files and raw simulation data are available from the corresponding author upon reasonable request.

References

[1] Giannini, V., Fernández-Domínguez, A.I., Heck, S.C. and Maier, S.A., 2011. Plasmonic nanoantennas: fundamentals and their use in controlling the radiative properties of nanoemitters. *Chemical Reviews*, *111*(6), pp.3888–3912.

[2] Schuller, J.A., Barnard, E.S., Cai, W., Jun, Y.C., White, J.S. and Brongersma, M.L., 2010. Plasmonics for extreme light concentration and manipulation. *Nature Materials*, *9*(3), pp.193–204.

[3] Desiatov, B., Goykhman, I. and Levy, U., 2011. Plasmonic nanofocusing of light in an integrated silicon photonics platform. *Optics Express*, *19*(14), p.13150.

[4] Valenti, M., Jonsson, M.P., Biskos, G., Schmidt-Ott, A. and Smith, W.A., 2016. Plasmonic nanoparticle-semiconductor composites for efficient solar water splitting. *Journal of Materials Chemistry A*, *4*(46), pp.17891–17912.

[5] Zhou, N., López-Puente, V., Wang, Q., Polavarapu, L., Pastoriza-Santos, I. and Xu, Q.-H., 2015. Plasmon-enhanced light harvesting: applications in enhanced photocatalysis, photodynamic therapy and photovoltaics. *RSC Advances*, *5*(37), pp.29076–29097.

[6] Conley, J.F., 2010. Instabilities in amorphous oxide semiconductor thin-film transistors. *IEEE Transactions on Device and Materials Reliability*, *10*(4), pp.460–475.

[7] Kamiya, T., Nomura, K. and Hosono, H., 2009. Origins of high mobility and low operation voltage of amorphous oxide TFTs: Electronic structure, electron transport, defects and doping. *Journal of display Technology*, *5*(7), pp.273-288.

[8] Seo, J. and Yoo, H., 2022. Zinc–tin oxide film as an earth-abundant material and its versatile applications to electronic and energy materials. *Membranes, 12*(5), p.485.

[9] Guo, L., Wang, Q., Wang, C., Chu, X., Hao, Y., Chi, Y. and Yang, X., 2024. Effect of Ga doping on the stability and optoelectronic properties of ZnSnO thin film transistor. *Micromachines, 15*(12), p.1445.

[10] Lee, J.H., Kim, C.H., Kim, H.S., Park, J.H., Ryu, J.H., Baek, K.-H. and Do, L.-M., 2013. Stability characteristics of gallium-doped zinc-tin-oxide thin-film transistors fabricated using a sol-gel method. *Journal of the Korean Physical Society, 62*(8), pp.1176–1182.

[11] Rycenga, M., Cobley, C.M., Zeng, J., Li, W., Moran, C.H., Zhang, Q., Qin, D. and Xia, Y., 2011. Controlling the synthesis and assembly of silver nanostructures for plasmonic applications. *Chemical Reviews, 111*(6), pp.3669–3712.

[12] Saini, I., Yadav, M. and others, 2020. Optoelectronic and sensing applications of plasmonic silver nanoparticles. *International Journal of Technical Research and Science, Special Issue*, pp.33–35.

[13] Sehmi, H.S., Langbein, W. and Muljarov, E.A., 2017. Optimizing the Drude–Lorentz model for material

permittivity: method, program, and examples for gold, silver, and copper. *Physical Review B*, *95*(11), p.115444.

[14] Batista, J.S. and El-Shenawee, M., 2021. 3D model of terahertz photoconductive antenna using COMSOL Multiphysics. *In: 2021 IEEE International Symposium on Antennas and Propagation (APS/URSI). Singapore: IEEE*, pp.1883–1884.

[15] Criollo, C. and Avila, A.G., 2015. Simulation of photoconductive antennas for terahertz radiation. *Ingeniería e Investigación*, *35*(1), pp.60–64.

[16] Tame, M.S., McEnery, K.R., Özdemir, Ş.K., Lee, J., Maier, S.A. and Kim, M.S., 2013. Quantum plasmonics. *Nature Physics*, *9*(6), pp.329–340.

[17] Volokitin, A.I. and Persson, B.N.J., 2017. Surface electromagnetic waves. In: Electromagnetic Fluctuations at the Nanoscale, NanoScience and Technology. Berlin: *Springer*, pp.21–27.

[18] Baltar, H.T.M.C.M., Drozdowicz-Tomsia, K. and Goldys, E.M., 2012. Propagating surface plasmons and dispersion relations for nanoscale multilayer metallic-dielectric films. In: K.Y. Kim, ed., *Plasmonics — Principles and Applications*. InTech.

[19] Cao, J., Balachandran, R., Keswani, M. and others, 2013. New plasmonic materials in visible spectrum through electrical charging. Proc. *SPIE OPTO, San Francisco, CA*, p.86321I.

[20] Salomon, L., De Fornel, F. and Goudonnet, J.P., 1991. Sample–tip coupling efficiencies of the photon-scanning tunneling microscope. *Journal of the Optical Society of America A*, *8*(12), p.2009.

[21] Mendoza Herrera, L.J., Arboleda, D.M., Schinca, D.C. and Scaffardi, L.B., 2014. Determination of plasma frequency, damping constant, and size distribution from the complex dielectric function of noble metal nanoparticles. *Journal of Applied Physics, 116*(23), p.233105.

[22] Lee, C.-G., Cobb, B. and Dodabalapur, A., 2010. Band transport and mobility edge in amorphous solution-processed zinc tin oxide thin-film transistors. *Applied Physics Letters, 97*(20), p.203505.

[23] Bao, Y. and Fang, Z., 2015. Plasmon-enhanced photodetection in nanostructures. *Nanotechnology Reviews*, 4.

[24] Chan, K., Wright, M., Elumalai, N., Uddin, A. and Pillai, S., 2017. Plasmonics in organic and perovskite solar cells: optical and electrical effects. *Advanced Optical Materials, 5*(3), p.1600698.

[25] Zapata-Cano, P.H., Moreno-Rodríguez, S., Amanatiadis, S., Alex-Amor, A., Zaharis, Z.D. and Molero, C., 2024. Transient states to control the electromagnetic response of space-time dispersive media. *Physical Review B, 110*, p.235125.

[26] Zhao, M., Li, H., He, Z., Chen, Z., Xu, H. and Zheng, M., 2017. Novel oscillator model with damping factor for plasmon induced transparency in waveguide systems. *Scientific Reports, 7*, p.10635.

[27] Chen, M.-I., Singh, A.K., Chiang, J.-L., Horng, R.-H. and Wuu, D.-S., 2020. Zinc gallium oxide — a review from synthesis to applications. *Nanomaterials, 10*(11), p.2208.

[28] Singh, R. and Ulrich, R.K., 1999. High and low dielectric constant materials. *The Electrochemical Society Interface, 8*(1), pp.26–30.

[29] Teng, J., Chen, Y., Huang, C., Yang, M., Zhu, B., Liu, W.-J., Ding, S.-J. and Wu, X., 2024. Graded-band-gap zinc–tin oxide thin-film transistors with a vertically stacked structure for wavelength-selective photodetection. *ACS Applied Materials & Interfaces, 16*(7), pp.9060–9067.

[30] Wu, C., Zhou, X. and Wei, J., 2015. Localized surface plasmon resonance of silver nanotriangles synthesized by a versatile solution reaction. *Nanoscale Research Letters, 10*, p.354.

[31] Zhao, N.Z., Williamson, I.A.D., Zhao, Z., Boutami, S. and Fan, S., 2019. Penetration depth reduction with plasmonic metafilms. *ACS Photonics, 6*(8), pp.2049–2055.

[32] Jia, X., Bowen, P., Huang, Z., Liu, X., Bingham, C. and Smith, D.R., 2018. Clarification of surface modes of a periodic nanopatch metasurface. *Optics Express, 26*(3), p.3004.

[33] Qi, X., Pérez, L.A., Alonso, M.I. and Mihi, A., 2024. High Q-factor plasmonic surface lattice resonances in colloidal nanoparticle arrays. *ACS Applied Materials & Interfaces, 16*(1), pp.1259–1267.

[34] Hu, C.-C., Wu, C.-H., Chien, C.-W., Kung, Y.-C., Chang, F.-M., Hsu, P.-C., Liao, C.-H., Lin, S.-I. and Wu, C.-C., 2010. High-performance oxide TFTs based on solution-processed ZTO. *In: 2010 IEEE Photonic Society's 23rd Annual Meeting. Denver, CO, USA: IEEE*, pp.311–312.

[35] Seo, S.-J., Choi, C.G., Hwang, Y.H. and Bae, B.-S., 2009. High performance solution-processed amorphous zinc tin oxide thin film transistor. *Journal of Physics D: Applied Physics, 42*(3), p.035106.

[36] Wang, I.-W., Shih, L.-C., Li, J.T. and Chen, J.-S., 2023. Analogy of photogating to voltage-gating in zinc-tin oxide thin-film transistor: efficiency and current saturation mechanism. *IEEE Transactions on Electron Devices, 70*(4), pp.1692–1696.

[37] Yang, C.-C., Tung, W.-J., Chang, S.-P., Hsu, M.-H., Huang, W.-L., Li, C.-H., Fang, Y.-J. and Chang, S.-J., 2018. Optical and photo-electrical properties of zinc tin oxide thin-film phototransistor. *In: 2018 7th International Symposium on Next Generation Electronics (ISNE). Taipei: IEEE*, pp.1–2.

[38] Lee, S. and Nathan, A., 2016. Conduction threshold in accumulation-mode InGaZnO thin film transistors. *Scientific Reports, 6*, p.22567.

[39] Vogt, K.T., Malmberg, C.E., Buchanan, J.C., Mattson, G.W., Brandt, G.M., Fast, D.B., Cheong, P.H.-Y., Wager, J.F. and Graham, M.W., 2020. Ultrabroadband density of states of amorphous In-Ga-Zn-O. *Physical Review Research, 2*(3), p.033358.

[40] Kim, J., Naik, G.V., Gavrilenko, A.V., Dondapati, K., Gavrilenko, V.I., Prokes, S.M., Glembocki, O.J., Shalaev, V.M. and Boltasseva, A., 2013. *Optical properties of gallium-doped zinc oxide — a low-loss plasmonic material: first-principles theory and experiment. Physical Review X, 3*(4), p.041037.

[41] Mantri, Y. and Jokerst, J.V., 2020. Engineering plasmonic nanoparticles for enhanced photoacoustic imaging. *ACS Nano, 14*(8), pp.9408–9422.

[42] Sistani, M., Bartmann, M.G., Güsken, N.A., Oulton, R.F., Keshmiri, H., Luong, M.A., Momtaz, Z.S., Den Hertog, M.I. and Lugstein, A., 2020. Plasmon-driven hot electron transfer at atomically sharp metal–semiconductor nanojunctions. *ACS Photonics, 7*(6), pp.1642–1648.

[43] Zhou, L., Huang, Q. and Xia, Y., 2024. Plasmon-induced hot electrons in nanostructured materials: generation, collection, and application to photochemistry. *Chemical Reviews, 124*(14), pp.8597–8619.